buildings

MDPI

Article

Finite Element Analysis and Calculation Method of Concrete-Filled Stainless Steel Tubes under Eccentric Tension

Wen-Chao Xie [1] and Yong Ye [1,2,*]

[1] College of Civil Engineering, Huaqiao University, Xiamen 361021, China; xwc@stu.hqu.edu.cn
[2] Key Laboratory for Structural Engineering and Disaster Prevention of Fujian Province, Xiamen 361021, China
* Correspondence: qzyeyong@hqu.edu.cn

Abstract: Concrete-filled stainless steel tubes (CFSST) could be used as structural members in corrosion-prone environments. A detailed numerical investigation of the mechanical performance and calculation method of CFSST members under eccentric tension is carried out in this paper. A finite element analysis (FEA) model that adopts three-dimensional elements is established, and related experimental results of CFSST and conventional concrete-filled carbon steel tubes (CFST) subjected to tension are used to validate the FEA model. Then, the calibrated FEA model is used to investigate the performance of CFSST eccentrically tensile members, especially the composite actions and stress distribution laws between the stainless steel tube and the concrete core, which play a key role in the load-carrying capacity of the composite member. To quantitatively determine the influence of different parameters on the load-carrying capacity of CFSST tensile members, a wide-range parametric analysis is performed. Finally, a calculation model is proposed to be used to predict the ultimate tensile strength of CFSST members subjected to eccentric tension, and the model-predicted values show good agreement with the FEA-computed results.

Keywords: concrete-filled stainless steel tube (CFSST); eccentric tension; finite element analysis; composite action; load-carrying capacity

Citation: Xie, W.-C.; Ye, Y. Finite Element Analysis and Calculation Method of Concrete-Filled Stainless Steel Tubes under Eccentric Tension. *Buildings* **2023**, *13*, 2757. https://doi.org/10.3390/buildings13112757

Academic Editor: Viorel Ungureanu

Received: 10 October 2023
Revised: 24 October 2023
Accepted: 29 October 2023
Published: 31 October 2023

1. Introduction

More and more scholars and architects are interested in concrete-filled stainless steel tubes (CFSST), primarily due to the superiority of their better corrosion resistance, higher durability, and wider application scenarios compared to concrete-filled steel tubes (CFSTs) incorporating carbon steel [1]. Increasing investigations have been conducted on the axial compression properties of CFSST short components with and without stiffeners [2–8], slender columns [9,10], and members with elliptical [11,12] and square cross sections [13]; the bending property of CFSST members [14–16]; the behavior of CFSST components under the combined loading conditions of compression and flexure [17–21]; and the capacity of CFSST components to resist lateral strike [22] or cyclic loading [23]. However, there is still a lack of comprehensive studies on the performance of CFSST components under tension, which would be encountered during the service life of engineering structures, especially under the conditions of severe earthquake or impact.

Besides the available limited study on the CFSST specimen's tensile performance, numerous studies have been completed to examine the mechanical properties of conventional CFST components under tensile loads [24–32]. The tension characteristics of CFST components, including cylindrical or square cross-sections, were examined by Han et al. [24], Li et al. [25], and Zhou et al. [26]. The results indicate that the ultimate load-carrying capacity of CFST components exhibits an approximate 10% increase compared to that of the matching hollow steel tubes. Li et al. [27,28] investigated the tensile properties of concrete-filled double-skin steel tube (CFDST) components. The findings revealed that the tensile capacity of CFDST components exhibited a significant increase compared to the hollow steel tubes because the sandwich concrete offered lateral bracing to the external steel tube. Han et al. [30] conducted experiments and FEA on the tensile properties of concrete-encased concrete-filled steel tube (CECFST) components. Wang et al. [29] researched the properties of circular CFST components reinforced with external CFRP sheets under the simultaneous influence of tension and bending. Chen et al. [31] studied the performance of reinforced CFST, which bears tensile loads. Xu et al. [32] presented calculation models that offer the capability to estimate the properties of CFST tensile components. Ye et al. [33] quantitatively evaluated the impact of concrete gaps on the reduction of tensile strength of CFST components through finite element simulation. Xie et al. [34] conducted a numerical study on concrete-filled bimetallic tubes (CFBT) tension specimens and proposed a model to predict the corresponding ultimate tensile capacity. The above research indicates that the steel–concrete combination effects actually enhance the tensile capacity of hollow steel tubes. The conclusion has significance, as it can serve as a valuable reference for investigating the behavior of CFSST eccentric tensile components.

Ye et al. [35,36] conducted experiments on 20 CFSST specimens to investigate their mechanical behavior and failure modes under concentric or eccentric tensile loads, numerical studies were also conducted, and a computational model was proposed for calculating the ultimate tensile capacity of axially loaded CFSST components. However, the composite interactions of stainless steel tube and concrete in eccentrically loaded CFSST members still need to be clarified, and so does the corresponding calculation approach of load-carrying capacity.

In light of the above research context, an FEA model is established to examine the performance of CFSST eccentrically tensile components herein. The research aims to achieve three primary objectives: (1) to construct a suitable FEA model that accurately simulates the full-range performance of CFSST eccentric tensile components; (2) to examine the impact of various parameters on the carrying capacity of CFSST eccentric tensile components; and (3) to provide a proper method for predicting the interaction between the axial tensile load (F) and bending moment (M) of CFSST members.

2. Numerical Modeling

2.1. General Information

2.1.1. Mesh Setting

The ABAQUS 2022 software is adopted to conduct the modeling. In the FEA model, each specimen is made up of a stainless steel tube, the core concrete, upper and lower endplates, and stiffeners between the tube and the endplates. The stainless steel tube and stiffeners are simulated by the S4R elements provided by ABAQUS, and the concrete core and endplates are simulated by the C3D8R elements. The primary surface in the interaction simulation between the stainless steel tube and concrete is defined as the inner side of the stainless steel tube, while the secondary surface is represented by the core concrete. In order to reduce the occurrence of node penetration and ensure that the model has good calculation accuracy and convergence, the mesh discretization of the primary surface is set as the same as that of the secondary surface, and the nodes of the primary and secondary surfaces coincide. To balance the calculation accuracy and efficiency, the unit mesh discretization is set as 16 mm based on the convergence analysis.

2.1.2. Interfacial Behavior

In the FEA model, relative slippage between the stainless steel tube and the concrete core is allowed at the contact interface, and "hard contact" is adopted in the normal direction. The Coulomb friction model is applied in the tangential direction, and an appropriate friction coefficient is selected. According to relevant research [1,37], the coefficient of friction on the stainless-steel–concrete interface decreases with the increase of relative interfacial displacement, and the friction coefficient ranges between 0.3 and 0.5. Thus, the friction coefficient in this research is taken as 0.3. Additionally, the stainless steel tubes, end plates, and stiffeners are all connected by the "tie" function in ABAQUS. In this paper, it is assumed that the end plate does not deform under ideal conditions, so the end plate was considered a rigid body and was not taken into account in the calculation.

2.1.3. Boundary Conditions

The established FEA model of CFFST members under eccentric tension is shown in Figure 1. The eccentric tension happens at the loading line on the top endplate. Additionally, all degrees of freedom, with the exception of x-axis rotation and z-axis translation, are constrained. A fixed line is set on the bottom outside of the lower endplate to constrain all the degrees of freedom, with the exception of the x-axis rotation.

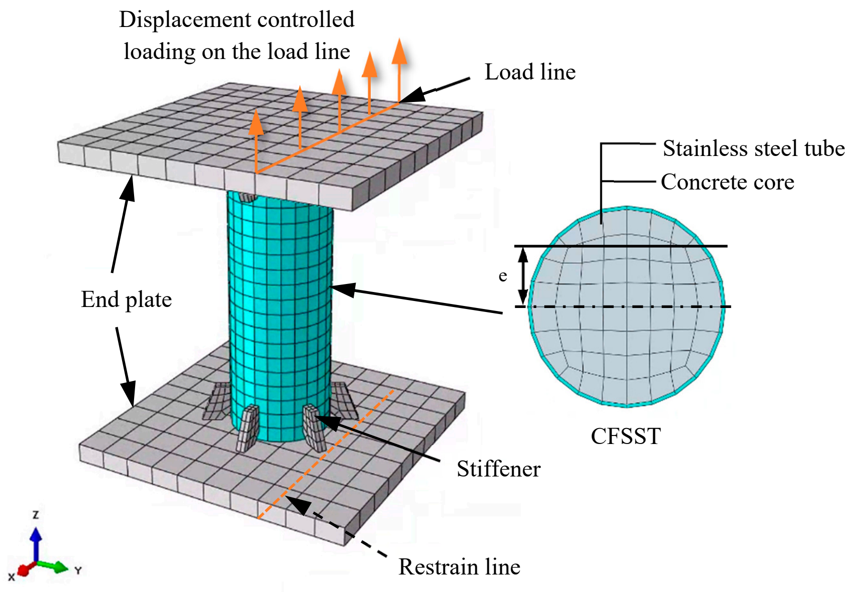

Figure 1. FEA model of CFSST member under eccentric tension.

2.2. Material Properties

2.2.1. Concrete

In the FEA model established herein, the constitutive response of concrete is simulated by the Concrete Damaged Plasticity Model, which includes two types of damage modes, i.e., compression crushing and tension cracking. The yield and failure surfaces are controlled by the equivalent compression and tensile plastic strains, respectively. For the compressive behavior of concrete, the stress-strain model established by Han [38] for simulating the compressive property of concrete confined by steel tubes is adopted, which considers the confined effect of steel tubes on concrete. According to the suggestion of the ACI 318 specification [39], the elastic modulus of concrete is set as $E_c = 4730\sqrt{f'_c}$, where f'_c is the cylinder compressive strength of concrete. As for the plastic parameters, the expansion angle is taken as 30° [40], the flow potential offset value is taken as 0.1, the ratio of biaxial/uniaxial strength (f_{b0}/f_{c0}) is taken as 1.16, and the viscosity factor is taken as 0.0001. The damage evolution parameters of core concrete are not considered in this paper.

The tensile property of core concrete is determined using a more convergent energy failure criterion [41], i.e., the cracking stress (σ_{t0}) versus fracture energy (G_F) relationship. The calculation formulas of σ_{t0} and G_F refer to related studies [28,42] and are as follows:

$$\sigma_{t0} = 0.26\left(1.25f'_c\right)^{2/3}, \tag{1}$$

$$G_F = 73f'^{0.18}_c. \tag{2}$$

2.2.2. Stainless Steel

Compared with carbon steel, the stress-strain relationship of stainless steel typically lacks a distinct yield stage.

Therefore, the modified Ramberg–Osgood model [43] is employed as the constitutive model for stainless steel within the FEA modeling, as shown in Figure 2. The model is considered the strain hardening index (n), and the value of n is adopted as the unified parameter value of the commonly used stainless steel types of building structures provided by Ashraf et al. [44]. The model has demonstrated high precision in reproducing the material response of stainless steel subjected to tensile loading.

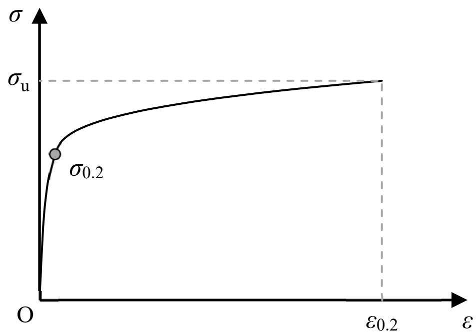

Figure 2. Stress–strain curves for stainless steel.

2.3. Model Validation

The test results of CFSST specimens under eccentric tension as reported in reference [35] are applied to verify the reliability of the established model. Table 1 presents the main parameters and corresponding verification outcomes. All the specimens have a length of 350 mm, with an outer diameter of 116 mm.

Table 1. Parameters and analysis results of eccentric tensile specimens.

Number	Specimen	t (mm)	e (mm)	$N_{u,e}$ (kN)	$M_{u,e}$ (kN·m)	$N_{u,FEA}$ (kN)	$M_{u,FEA}$ (kN·m)	$N_{u,FEA}/N_{u,e}$	$M_{u,FEA}/M_{u,e}$
1	t2-e50	2.0	50	98.1	5.0	96.4	4.8	0.97	0.96
2	t2-C50-e25-1	2.0	25	135.6	3.4	145.2	3.6	1.07	1.05
3	t2-C50-e25-2	2.0	25	134.7	3.3	145.2	3.6	1.08	1.09
4	t2-C50-e50-1	2.0	50	130.0	6.5	102.4	5.1	0.78	0.78
5	t2-C50-e50-2	2.0	50	99.0	5.0	102.4	5.1	1.03	1.02
6	t2-C50-e75-1	2.0	75	95.5	7.2	96.7	7.3	1.01	1.01
7	t2-C50-e75-2	2.0	75	91.2	6.8	96.7	7.3	1.06	1.07
8	t3-e50	3.0	50	155.5	7.8	149.4	7.5	0.96	0.96
9	t3-C50-e25	3.0	25	173.4	4.3	176.8	4.4	1.02	1.02
10	t3-C50-e50	3.0	50	164.6	8.2	169.8	8.5	1.03	1.04
11	t3-C50-e75	3.0	75	126.3	9.5	129.6	9.7	1.03	1.02

Note: average $N_{u,FEA}/N_{u,e}$ = 1.004; Standard deviation $N_{u,FEA}/N_{u,e}$ = 0.079; average $M_{u,FEA}/M_{u,e}$ = 1.002; Standard deviation $M_{u,FEA}/M_{u,e}$ = 0.080.

The deformation patterns of the FEA models and the experimental specimens are compared in Figure 3, where the CFSST model (t2-C50-e50) and the hollow stainless steel tube model (t2-e50) are selected as the reference. It can be seen that both the t2-e50 and t2-C50-e50 models experience overall bending deformation, and the t2-e50 model shows the concave deformation generated in the middle. The plastic deformation of the core concrete is depicted in Figure 3c, where the vertical direction of the red arrows indicates the cracking direction on the surface of core concrete. The comparison results show that the deformation patterns of FEA models are in favorable consistency with the experimental outcomes. Table 1 and Figure 3 show that the presence of core concrete significantly improves the ability of CFSST specimens to bear eccentric tensile loads compared with hollow steel tube specimens, and the deformation modes are significantly different.

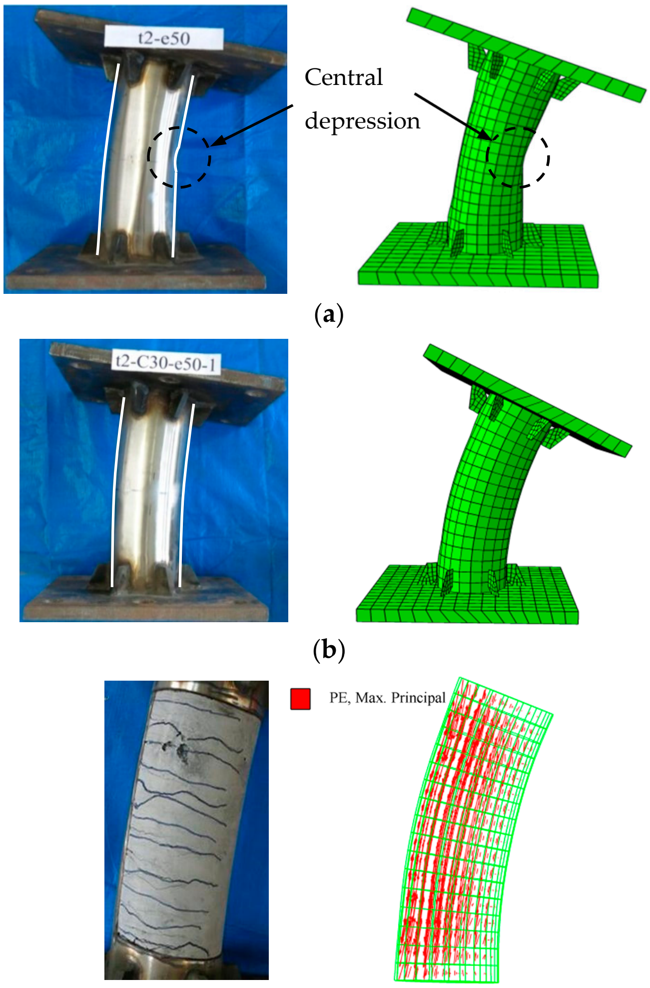

(**c**)

Figure 3. Comparison between predicted and experimental results under eccentric tensile: (**a**) t2 (ST); (**b**) t2-C50 (CFSST); (**c**) t2-C50 (Core concrete).

Figure 4 shows the comparison of the load (F)-displacement (Δ) relations between the FEA predictions and the experimental test findings. The FEA-predicted F-Δ curves are generally in good agreement with the experimentally obtained ones under different parameters. Table 1 presents the comparison between the ultimate tensile strength ($F_{\mathrm{u,FEA}}$) and the corresponding bending moment ($M_{\mathrm{u,FEA}}$) predicted by the FEA modeling and the values obtained from experimental measurements. The average error between the predicted ultimate tensile strengths and the test measurements is 4.2%, and the average error between the predicted ultimate bending moments and the test measurements is 4.3%. Thus, the FEA model demonstrates a significant level of precision in predicting the load strength of eccentrically tension-loaded CFSST specimens and could be used to further investigate the same type of steel–concrete composite members.

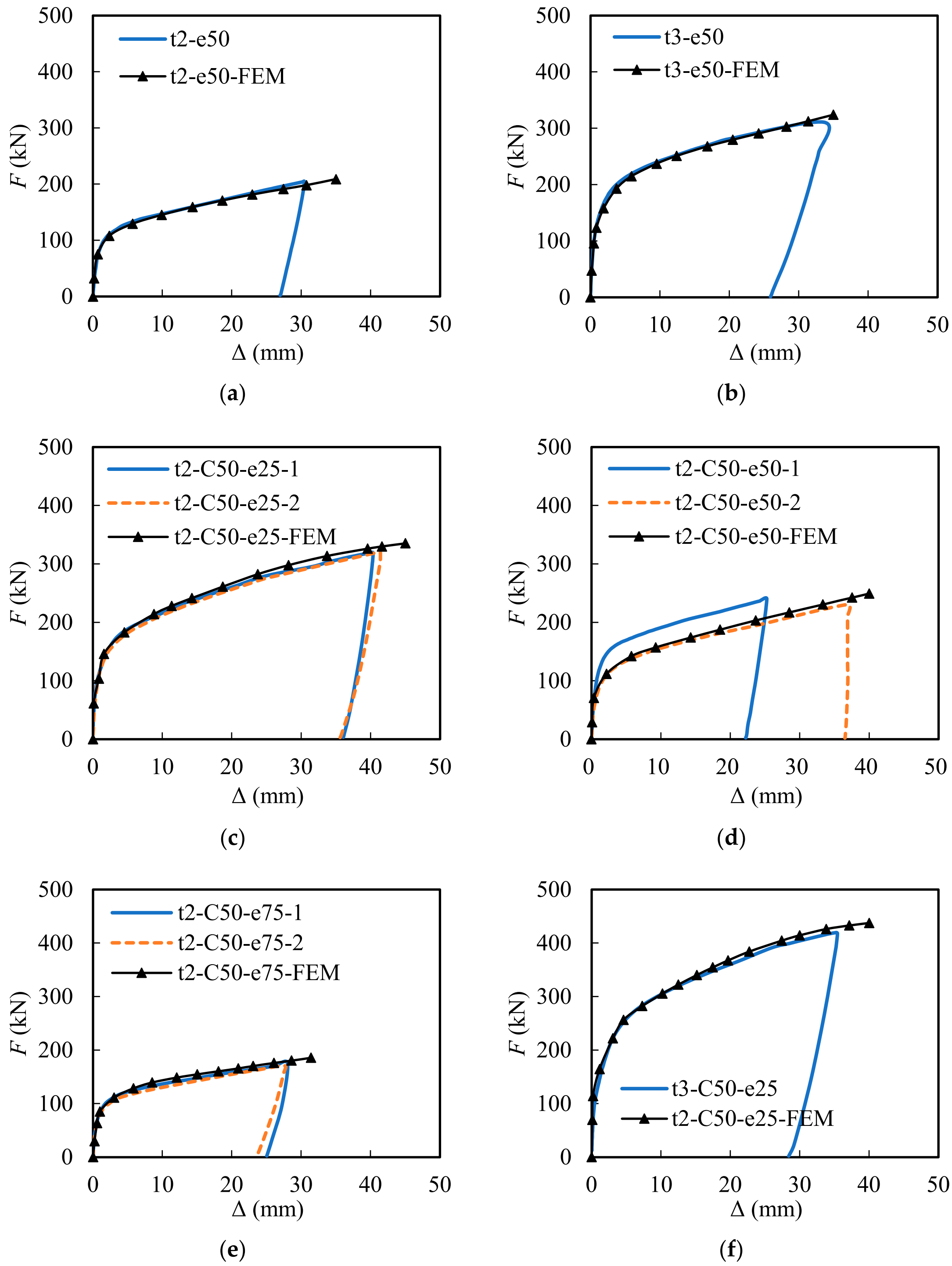

Figure 4. *Cont.*

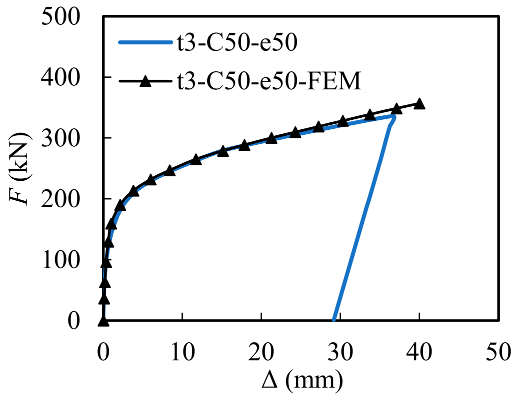

(**g**)

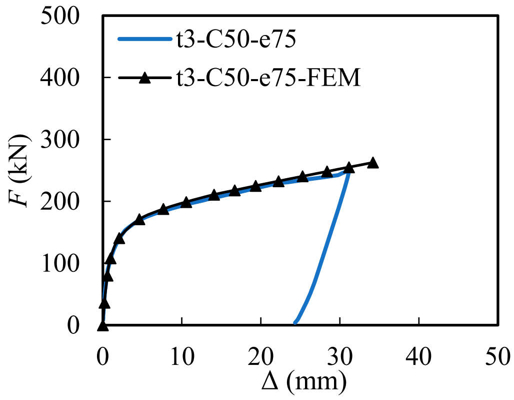

(**h**)

Figure 4. Comparison between predicted and experimental *F*-Δ curves: (**a**) t2-e50; (**b**) t3-e50; (**c**) t2-C50-e25; (**d**) t2-C50-e50; (**e**) t2-C50-e75; (**f**) t3-C50-e25; (**g**) t3-C50-e50; (**h**) t3-C50-e75.

3. Analytical Behavior and Discussion

Typical parameters are set for further analysis of CFSST members under eccentric tension, as follows: outer diameter of stainless steel tube D = 400 mm; length L = 1200 mm (corresponding L/D = 3.0); eccentricity ratio e/D = 0.5; steel ratio α = 0.108; nominal yield stress of stainless steel $\sigma_{0\cdot 2}$ = 300 MPa; elastic modulus of stainless steel E_s = 200 GPa; strain hardening index of stainless steel n = 5; cubic compressive strength of concrete f_{cu} = 50 MPa; elastic modulus of concrete E_c = 34.5 GPa.

3.1. Deformation Response under Loading

The overall shape of the load (F) versus displacement (Δ) curve and the moment (M)-rotation angle (θ) curve of CFSST components are basically similar, and both can nearly be categorized into five stages through five points (A, B, C, D, and E), as shown in Figure 5.

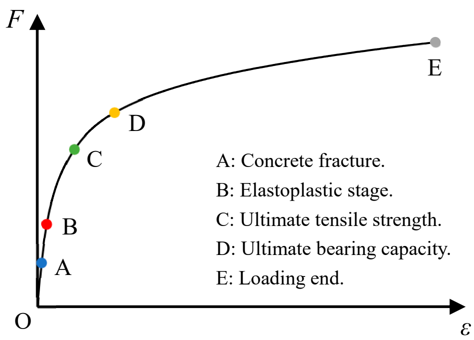

Figure 5. Characteristic points on tension-elongation curve of CFBT member.

Stage 1 (from Point O to Point A). At Stage OA, the applied tensile load improves linearly with the increase of displacement, and the member behaves elastically. The stage length shortens as the load eccentricity increases.

Stage 2 (from Point A to Point B). The stiffness of the CFSST member decreases slightly, and the whole member behaves approximately elastically. The tensile region of concrete core cracks, and the tensile stress within the region is mainly carried by the stainless steel. The concrete core provides lateral support to the stainless steel tube and also carries compressive stress with the compressive region of the CFSST member.

Stage 3 (from Point B to Point C). The stiffness of the specimen exhibits a notable drop as the deformation increases, and the CFSST member enters the elastic-plastic stage. The maximum longitudinal strain of stainless steel in the tension region reaches 5000 με at point C, which is considered the limit point of CFSST members under concentric tension.

Stage 4 (from Point C to Point D). The slope of the curve almost remains stable, and the load continues to increase at a much smaller rate than in the previous stages. The maximum tensile strain of stainless steel reaches 10,000 με at point D, which is considered the limit point of CFSST members under eccentric tension and pure bending.

Stage 5 (from Point D to Point E). The stiffness change of the F-ε relation tends to be gentle, and the load growth rate is smaller than in the previous four stages. When the loading ends at Point E, the overall bending deformation of CFSST members is obvious.

3.2. Force Distribution between Steel Tube and Concrete

The internal force allocation between various components of a typical model under an eccentric tensile load of 200 kN is shown in Figure 6, where N represents the load subjected by the stainless steel or concrete during loading, N_t represents the load carried by the CFSST specimen, and ε is the maximum longitudinal tensile strain of stainless steel tube. The figure indicates that the proportion of the load borne by the steel tube shows an overall upward trend with the increase of load eccentricity. In Stage OA, the steel tube deforms after the external load is applied, and then the partial load is transferred to the core concrete through the stainless-steel–concrete interface. When the strain value reaches 575 με (Point A), the concrete cracks, and the proportion of loading subjected by the concrete starts to decrease, while the proportion of load borne by the stainless steel tube experiences an increase. As the strain reaches 1311 με (Point B), the stainless steel tube enters the elastic-plastic stage, and the increasing ratio of load slows down. When the maximum strain of the steel tube reaches 5000 με (Point C), the tension ratio of the stainless steel tube is 1.1, and the core concrete ratio is −0.1. This is because after the formation of cracks in the tension region of the concrete, the axial tensile force borne by the concrete decreases rapidly. The core concrete in the pressure region transfers the load through the end plates to provide longitudinal support for the stainless steel tube, so the ratio of N/N_t for the stainless steel tube is greater than 1.

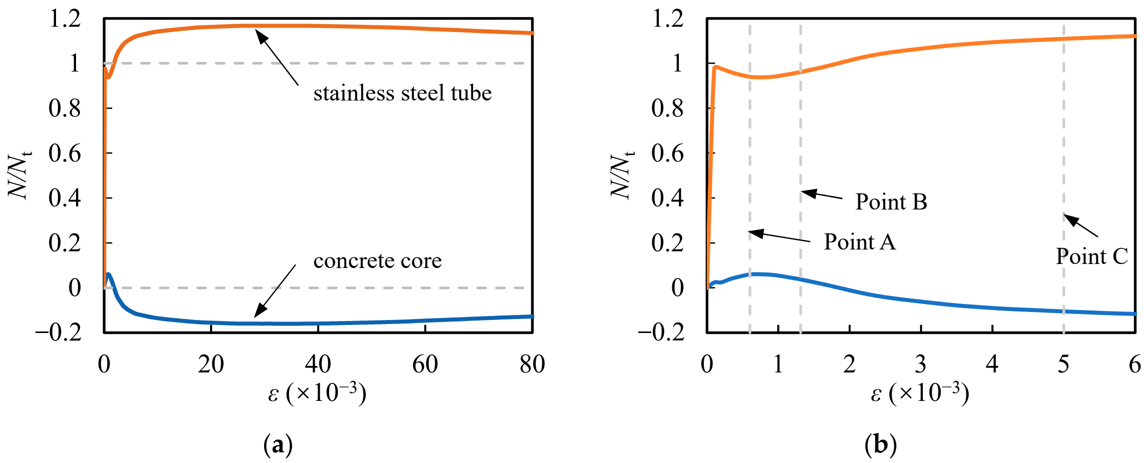

Figure 6. Load distributions of CFSST member under eccentric tension: (**a**) Whole process; (**b**) Initial stage.

3.3. Contact Stress of Stainless Steel Tube-Concrete Core Interface

When the CFSST specimens are under eccentric tension, the member undergoes bending deformation, and the stainless steel tube and concrete are squeezed against each other, resulting in an interaction between the two components. There are tension parts and compression parts in the CFSST specimen. Take three points on the middle section of the CFSST specimen, as depicted in Figure 7. Point 1 represents a point in the tension area, Point 2 represents a point in the neutral surface area, and Point 3 represents a point in the compression area of the model. The development of contact stress of stainless-steel–concrete interface in CFSST specimen under typical parameters is shown in Figure 8. In

Stage OA, the two components jointly bear the tensile force, and the stainless-steel–concrete interface contact stresses at Points 1, 2, and 3 all increase with the increase in strain. In the AB stage, the core concrete cracks when the strain reaches point A. In the core concrete model herein, the concrete that reaches its ultimate tensile strain will not crack. At the same position, the longitudinal strain value of the concrete will increase rapidly, and obvious radial shrinkage will occur. At this time, the stainless steel tube is in the elastic stage, the stainless-steel–concrete interface contact stress has a tendency to separate, and the contact stress at the three points begins to decrease significantly. In Stage BC, the stainless steel at Points 1 and 2 began to enter the plastic stage successively. The radial shrinkage of the steel tube increased, so it began contact with the concrete again and generated contact pressure. When the strain reaches 2417 με, the compressive load at Point 3 further increases, causing a dent inward and contacting the core concrete again. The main function of the core concrete is to offer lateral support to the steel tube, so the interface contact stress rises again.

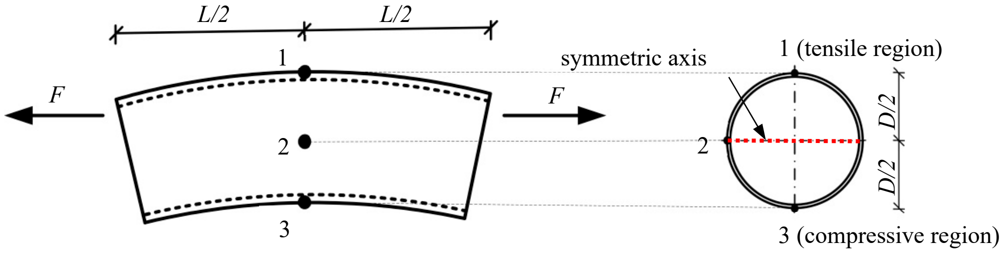

Figure 7. Location of contact stress of FEA model.

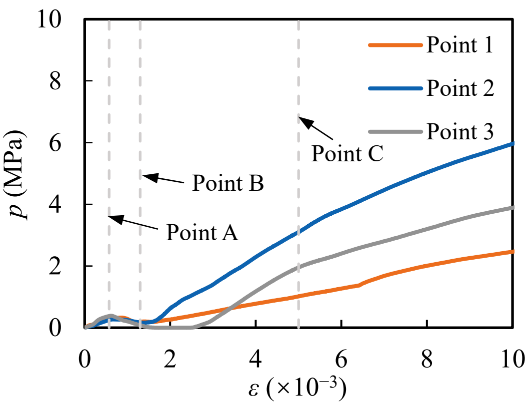

Figure 8. Contact stress (p) versus strain (ε) curves.

When the strain develops to Point C, the position of Point 1 is under extreme tensile load, so the width and number of concrete cracks here are the largest, and the interface contact stress is small. The width and number of concrete cracks at Point 2 are less than those at Point 1. The contact stress produced at the interface between steel tube and concrete decreases from Point 2 to Point 3 and then to Point 1.

3.4. Stainless Steel Tube Stress

For the eccentric tensile specimen under typical parameters (e = 200 mm), the deformation characteristics of the middle region of the CFSST specimen are the most significant, so the stainless steel tube in the middle part is studied. The longitudinal stress development is shown in Figure 9, where h is the distance to the extreme compressive side. For the specimen with e/D = 0.5, the longitudinal stress in the tension region of the stainless steel tube develops faster than that in the compression region. The distribution areas of the tensile and compressive stresses almost keep constant. The neutral axis is approximately at h/H = 0.188. The stress development of stainless steel tube can also be partitioned into five stages corresponding to the deformation response of CFSST specimens. In Stage OA and AB, the stainless steel is still in the elastic section, and the stainless steel stress changes at each section height are almost linear. In Stage BC, the stainless steel tube in the tension section enters the elastic-plastic stage from high to low along the cross-sectional height, and the growth rate of the longitudinal stress in the extreme tension region slows down significantly. At the end of this stage (Point C), the maximum stress of the stainless steel tube reaches yield. At this time, the longitudinal stress of the stainless steel in the pressure region is −146.09 MPa. In Stage CD, the longitudinal stress in the extreme tensile region continues to grow, and the growth trend slows down significantly. The yield zone of the stainless steel tube develops to near the middle of the section. At Point D, the stress in the extreme tension zone is 383.64 MPa, and the stress in the extreme pressure zone is −185.11 MPa.

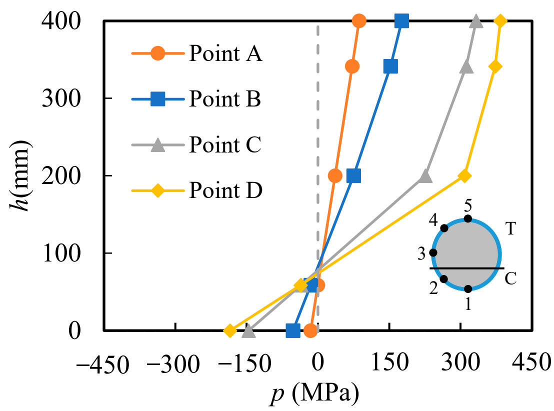

Figure 9. Longitudinal stress of stainless steel tube at mid-height.

Figure 10 illustrates the stress path on the tension side of a stainless steel tube, the variables $\sigma_{s,l}$, $\sigma_{s,t}$, and $\sigma_{s,Mises}$ represent the longitudinal stress, transverse stress, and von Mises stress, respectively. For CFSST specimens under eccentric tension, the inner concrete laterally supports for the stainless steel tube to resist radial shrinkage deformation, so simultaneous generation of $\sigma_{s,l}$ and $\sigma_{s,l}$ occurs in the stainless steel tube. The stress path change is the same as the von Mises criterion after the stainless steel yields. When the strain in the middle of the component reaches Point C, the value of $\sigma_{s,l}$ is approximately $1.1f_y$ under the combined action.

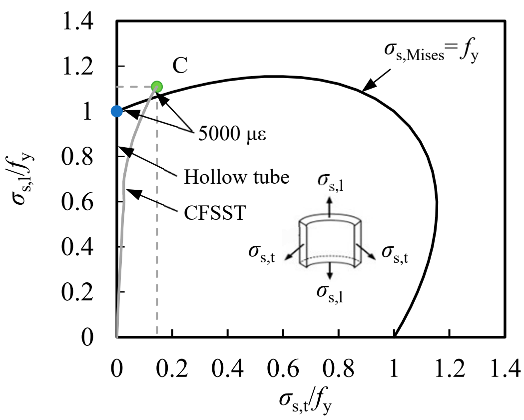

Figure 10. Composite effect in CFSST tensile member.

3.5. Concrete Stress

In the CFSST members under eccentric tension, the concrete core can be divided into tension and compression zones based on the stress states. Adopting typical parameters, the distribution of longitudinal stress (S33) in the middle section of the core concrete at different stages is shown in Figure 11, where the position of the dotted line is same as the neutral axis. As the eccentric tensile load increases, the position of the neutral axis tends to move closer to the edge of the concrete, indicating that the area of tension zone continues to increase. At the end of Stage OA, the maximum tensile stress endured by the core concrete is 3.34 MPa. After reaching the peak tensile stress, cracks begin to form in the tension zone of concrete. The maximum compressive stress endured by the concrete in the compression region is 5.99 MPa. In Stage AB, the number of cracks in the tension region increases, the location of neutral axis approaches the compression side, and the maximum stress in the compressive region increases to 11.89 MPa at Point B. In Stage BC, the position of neutral axis continues to approach the compression zone. The maximum compressive stress endured by concrete at Point C is 21.85 MPa. In Stage CD, the location of neutral axis is almost unchanged, and the maximum compressive stress develops to 34.99 MPa at Point D.

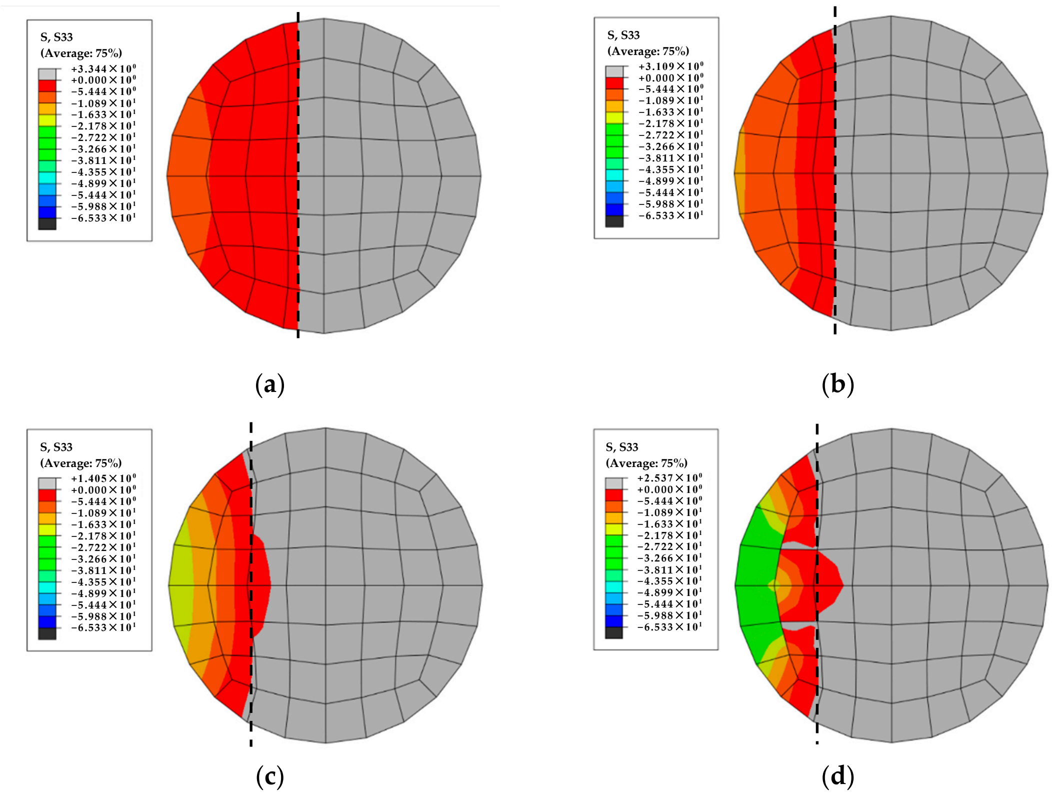

Figure 11. Distribution of longitudinal stress (S33) in concrete core at different stages: (**a**) Point A; (**b**) Point B; (**c**) Point C; (**d**) Point D.

4. Parametric Investigate

The validated FEA model is employed to study the impact of various parameters on the bearing capacity of CFSST specimens subjected to eccentric tension. Previous studies have shown that the n of stainless steel and the μ of stainless-steel–concrete interface have a minor influence on the bearing capacity of CFSST specimens under axial tension [36]. Hence, the parameters considered in this section include α = 0.041–0.235; e/D = 0–1.5; $\sigma_{0 \cdot 2}$ = 200–600 MPa; and f_{cu} = 30–80 MPa.

4.1. Effect of Stainless Steel Ratio

Based on the force distribution laws of CFSST members as described in the above section, the steel ratio (α) is expected to have a significant influence on the tensile properties of CFSST short columns because the externally applied tensile loading is primarily borne by the stainless steel tube. The influence of α on the F-ε response and ultimate tensile capacity (F_u) of eccentrically loaded CFSST members are shown in Figures 12 and 13, where the α-value ranges between 0.041 and 0.235, the value of e/D equals 1/2, and the other parameters are taken the same as the typical CFSST member. The data presented in Figure 12 exhibits a clear trend in the ultimate tensile capacity of CFSST specimens, showing a nearly linear rise as the α-value varies within the considered range.

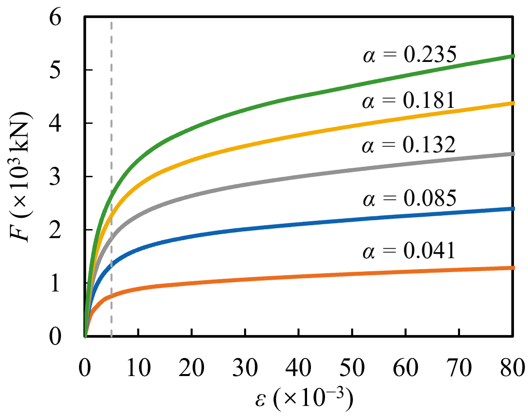

Figure 12. Effect of α on the F-ε curves.

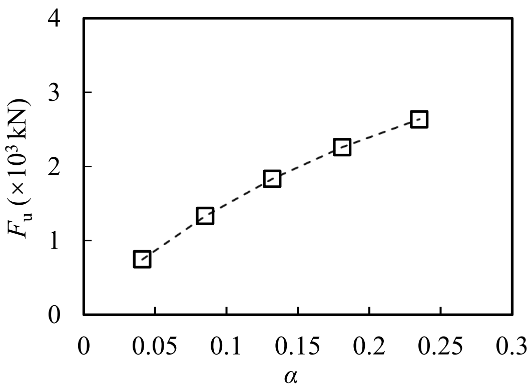

Figure 13. Effect of α on F_u.

4.2. Effect of Load Eccentricity

In order to research the effect of load eccentricity (e) on the F_u-value of CFSST members, the eccentricity ratio e/D = 0–1.5 is kept constant and the other parameters are taken the same as the typical CFSST member. Figure 14 shows the load (F)-strain (ε) response of CFSST members with different e/D-values. As the eccentricity ratio increases, the F_u-value of CFSST members shows a gradually decreasing trend. Compared with the concentric tensile short columns, the F_u-value of CFSST short columns with an e/D-value of 1/4, 1/2, 3/4, 1, 5/4, and 3/2 decreased by 43.7%, 61.3%, 70.2%, 76.1%, 80.0,% and 82.9%, as shown in Figure 15.

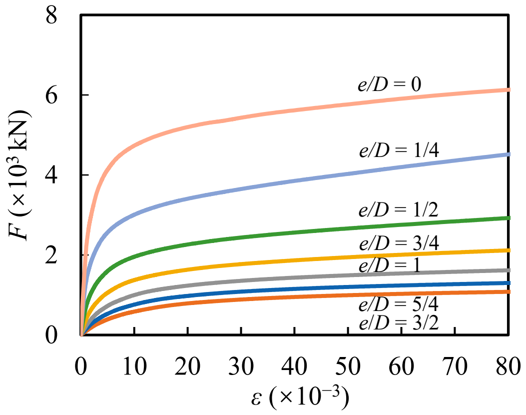

Figure 14. Effect of e/D on the F-ε curves.

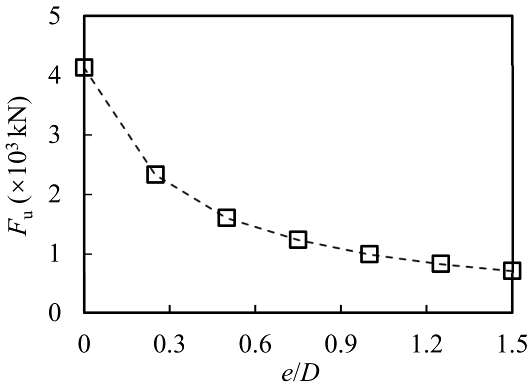

Figure 15. Effect of e/D on F_u.

4.3. Effect of Stainless Steel Strength

Figure 16 shows the effect of the $\sigma_{0 \cdot 2}$-value on the F_u-value of eccentrically loaded CFSST members. The load eccentricity is set at 1/2, the strain hardening index is set at 5 [44], and the other parameters are the same as the typical CFSST member. As the $\sigma_{0 \cdot 2}$-value increases from 200 MPa to 600 MPa, the F_u-value of eccentrically loaded CFSST short columns increases almost linearly, as shown in Figure 17.

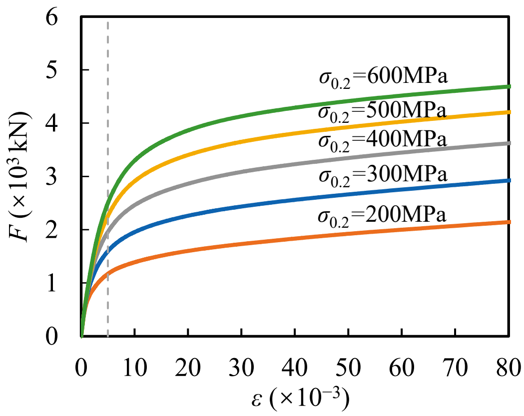

Figure 16. Effect of $\sigma_{0 \cdot 2}$ on the F-ε curves.

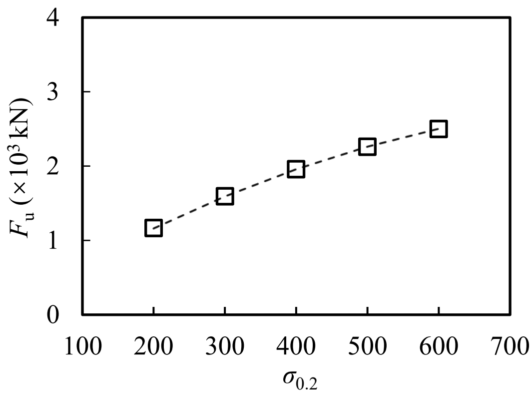

Figure 17. Effect of $\sigma_{0 \cdot 2}$ on F_u.

4.4. Effect of Concrete Strength

Figure 18 depicts the influence of f_{cu}-values on the F-ε curve of CFSST eccentric tension short columns. The f_{cu}-values vary from 30–80 MPa, and the remaining parameters are the same as the typical CFSST member. In Figure 19, the simulation results show that the ultimate tensile strength (F_u) with a f_{cu}-value of 80 MPa is only increased by 3.3% compared to that with a f_{cu}-value of 30 MPa, so the impact of concrete strength on the ultimate tensile capacity of CFSST eccentric tension short columns is nearly inappreciable.

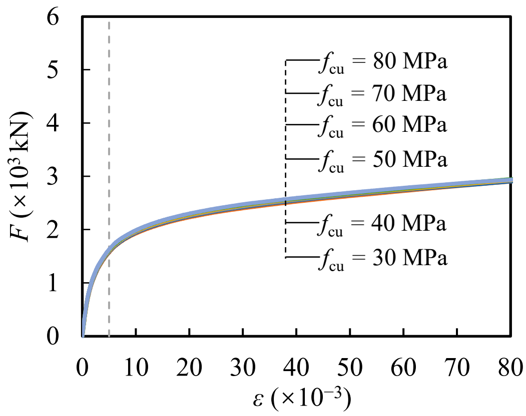

Figure 18. Effect of f_{cu} on the F-ε curves.

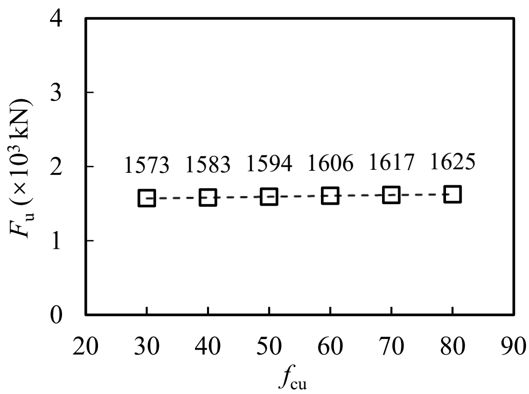

Figure 19. Effect of f_{cu} on F_u.

5. Calculation Model

The critical issues related to the design of CFSST members mainly include the ultimate tensile capacity, the flexural capacity, and the composite action between axial tension and bending moment. Currently, there is no relevant formula for calculating the tensile capacity of CFSST columns under eccentric tension. The Chinese Code DBJ/T13-51-2010 [45] suggests that the interaction curve between tensile force and bending moment of CFST members adopts a linear relationship, and the equation for computing the interaction relationship between tensile load (F) and bending moment (M) can be stated as follows:

$$\frac{F}{F_u} + \frac{M}{M_u} \leq 1, \tag{3}$$

$$F \leq F_u, \tag{4}$$

where F_u and M_u are the ultimate tensile strength and bending strength.

The FEA-calculated F-M interaction curve for CFSST members with a steel ratio (α) of 0.1 is depicted in Figure 20, where the predicted tensile strength (F_{FEA}) and bending strength (M_{FEA}) are normalized by the $F_{u\text{-}FEA}$ of the concentrically loaded members and the $M_{u\text{-}FEA}$ of the pure bending members. It can be seen that the F-M interaction basically follows the linear relationship described in Equation (3), but there is still a certain deviation, especially for the members with a load eccentricity (e/D) exceeding 0.25.

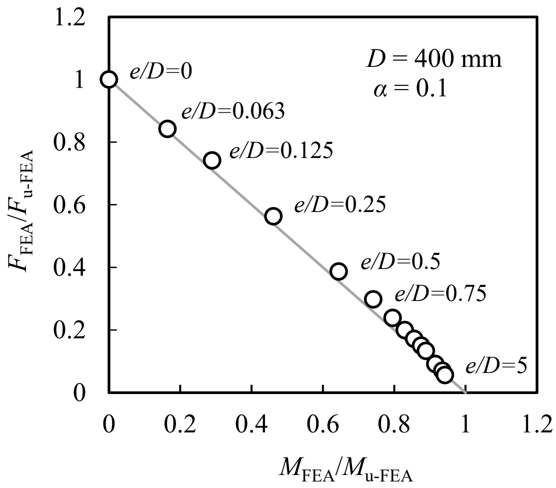

Figure 20. Tension-bending interaction curve.

The maximum tensile strain of stainless steel corresponding to F_u and M_u in Equation (3) is 5000 με and 10,000 με, which are different from each other. Considering the normal use requirements of the CFSST members, it is recommended that the ultimate load-carrying strength of the CFSST eccentrically tensile members is taken as the load when the maximum tensile strain of stainless steel reaches 10,000 με. We regress the finite element simulation results of the CFSST tension members in Figure 20 under different eccentricities. The regression results are used to modify Equation (3), and the load (F)-bending moment (M) interaction equation of the CFSST eccentric member is obtained, which is expressed as:

$$\left(\frac{F}{\delta F_{u-5k}}\right)^{1.15} + \frac{M}{M_u} \leq 1, \tag{5}$$

where the ultimate tensile strength ($F_{u\text{-}5k}$) and bending strength (M_u) both correspond to a maximum steel strain of 10,000 με; δ is the relationship coefficient between $F_{u\text{-}10k}$ and $F_{u\text{-}5k}$.

Han et al. [24] presented a formula to predict the bearing capacity of CFST tensile members, and the formula considered the contribution of the concrete core. Ye et al. [36] found that the prediction of CFSST tensile strength with the above model showed a significant deviation. As a result, Ye et al. [36] studied the F_u of CFSST members through

FEA simulation, and an improved model was suggested for the CFSST tensile members as follows:

$$F_{\mathrm{u-5k}} = \psi A_{\mathrm{s}} \sigma_{0.2}, \tag{6}$$

where ψ is the coefficient considering the effect of α and $\sigma_{0.2}$, and $\psi = 1.121\beta_{\alpha}\beta_{\sigma_{0.2}}$, $\beta_{\alpha} = 1.1418 - 1.2087\alpha$, and $\beta_{\sigma_{0.2}} = 1.1719 - 0.0006\sigma_{0.2}$.

Within the range of parameters considered in this paper, the tensile strengths of CFSST members at 5000 με and 10,000 με are obtained by finite element simulation. The relationship between the two values is shown in Figure 21. It can be seen that the two values basically follow a positive linear relationship, and the corresponding coefficient between them (δ) equals approximately 1.1469. Based on Equation (5), the equation for calculating the ultimate tensile capacity of concentrically loaded CFSST members corresponding to a maximum steel strain of 10,000 με is proposed as follows:

$$F_{\mathrm{u-10k}} = \delta \psi A_{\mathrm{s}} \sigma_{0.2} \tag{7}$$

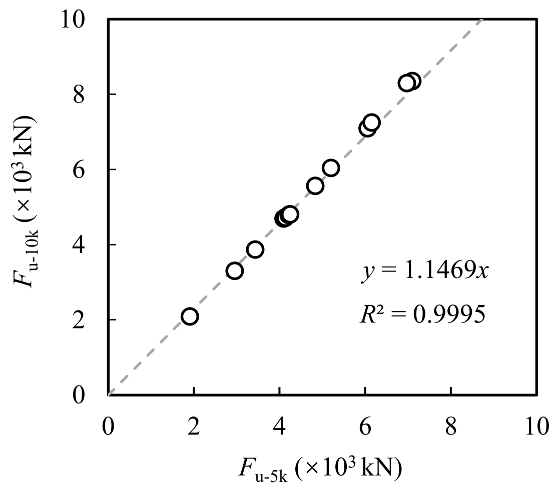

Figure 21. $F_{\mathrm{u\text{-}5k}}$- $F_{\mathrm{u\text{-}10k}}$ curve.

The comparison between the *F-M* curve predicted by Equation (5) and the finite element analysis results of typical parameter specimens is shown in Figure 22a. The average deviation between the predicted results and the FEA calculation results is 0.49%, and the standard deviation is 0.010. The parameter analysis results show that the steel ratio (α) and the stainless steel yield strength ($\sigma_{0\cdot2}$) are important factors affecting the bearing capacity of CFSST eccentric members. Therefore, the prediction results under different eccentricities and different stainless steel yield strengths are analyzed. The comparison between the prediction results of Equation (5) and the FEA calculation results of α = 0.041–0.235 specimens and $\sigma_{0\cdot2}$ = 200–600 MPa specimens is depicted in Figure 22b,c, respectively. Within the considered α-value range, the average deviation between the predicted results and the FEA calculation results is 1.81%, and the standard deviation is 0.013. Within the considered $\sigma_{0\cdot2}$-value range, the average deviation between the prediction results and the FEA calculation results is 1.35%, and the standard deviation is 0.016. As a result, the above-revised formula has good prediction accuracy for the *F-M* interaction relationship of CFSST eccentrically tensile members.

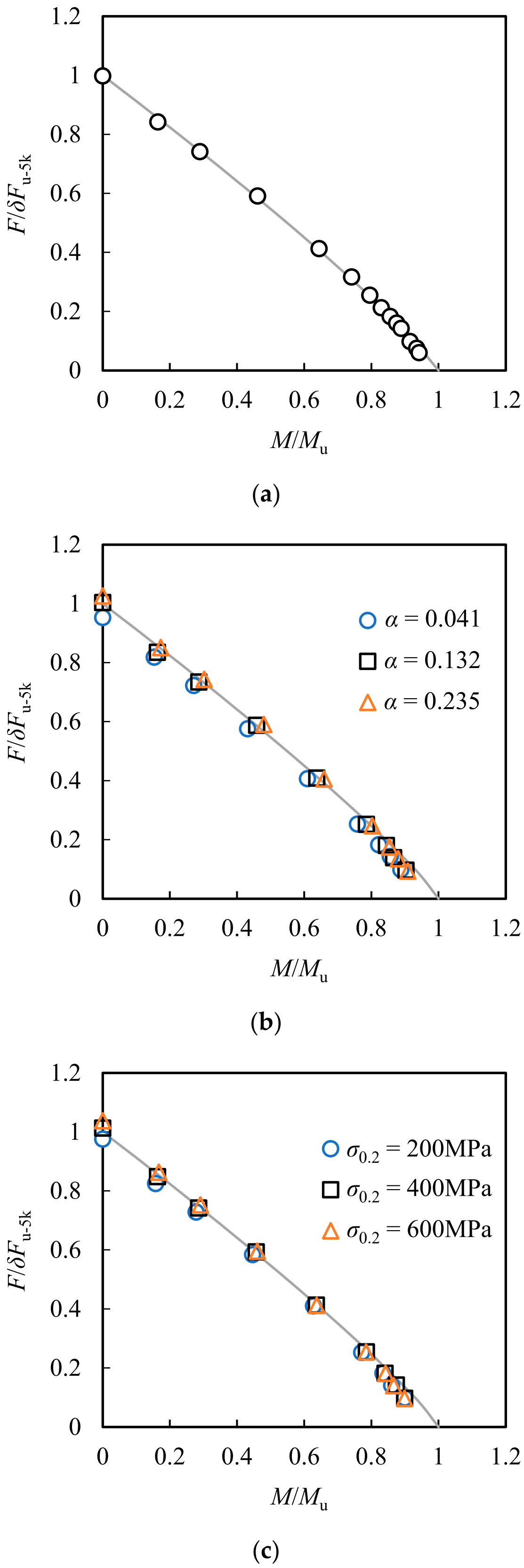

Figure 22. Comparison of formula-predicted and FEA-computed results: (**a**) α = 0.1, $\sigma_{0.2}$ = 300 MPa; (**b**) α = 0.041–0.235, $\sigma_{0.2}$ = 300 MPa; (**c**) α = 0.1, $\sigma_{0.2}$ = 200–600 MPa.

6. Conclusions

The researchers employ FEA simulation to research the response of CFSST eccentrically tensile members herein. Based on the parameters under considered range, the following conclusions could be drawn:

1. Considerable accuracy has been achieved in calculating the mechanical property of CFSST eccentrically tensile members using the established FEA three-dimensional model;
2. The analysis confirms the combined actions of the stainless steel tube and core concrete are necessary when calculating the ultimate strength of CFSST eccentrically tensile members;
3. The steel ratio, 0.2% proof stress of stainless steel ($\sigma_{0.2}$), and load eccentricity play the key role in the ultimate load-carrying capacity of CFSST tensile members. While the influence of concrete strength is inappreciable in the range of concrete strength parameters considered;
4. This study presents a reliable model for the prediction of the ultimate load-carrying capacity of CFSST members under eccentric tension, and acceptable conformance is accomplished between the formula-predicted and FEA-calculated results with minor error and scatter.

Author Contributions: Writing—original draft preparation and formal analysis, W.-C.X.; conceptualization, methodology, and writing—review and editing, Y.Y. All authors have read and agreed to the published version of the manuscript.

Funding: This research was funded by the National Natural Science Foundation of China (Grant No. 52278182) and the Natural Science Foundation of Fujian Province, China (Grant No. 2021J01286).

Data Availability Statement: The data used to support the findings of this research are available from the corresponding author upon request.

Acknowledgments: This research is supported by the National Natural Science Foundation of China (Grant No. 52278182) and the Natural Science Foundation of Fujian Province, China (Grant No. 2021J01286). The support is highly appreciated.

Conflicts of Interest: The authors declare no conflict of interest.

References

1. Han, L.H.; Xu, C.Y.; Tao, Z. Performance of concrete filled stainless steel tubular (CFSST) columns and joints: Summary of recent research. *J. Constr. Steel Res.* **2019**, *152*, 117–131. [CrossRef]
2. Young, B.; Ellobody, E. Experimental investigation of concrete-filled cold-formed high strength stainless steel tube columns. *J. Constr. Steel Res.* **2006**, *62*, 484–492. [CrossRef]
3. Ellobody, E.; Young, B. Design and behaviour of concrete-filled cold-formed stainless steel tube columns. *Eng. Struct.* **2006**, *28*, 716–728. [CrossRef]
4. Lam, D.; Gardner, L. Structural design of stainless steel concrete filled columns. *J. Constr. Steel Res.* **2008**, *64*, 1275–1282. [CrossRef]
5. Hassanein, M.F. Numerical modelling of concrete-filled lean duplex slender stainless steel tubular stub columns. *J. Constr. Steel Res.* **2010**, *66*, 1057–1068. [CrossRef]
6. An, H.; Wang, F.; Zhao, O. Experimental and numerical studies of concrete-filled high-chromium stainless steel tube (CFHSST) stub columns. *Thin-Walled Struct.* **2019**, *2019*, 106273.
7. Dabaon, M.A.; El-Boghdadi, M.H.; Hassanein, M.F. Experimental investigation on concrete-filled stainless steel stiffened tubular stub columns. *Eng. Struct.* **2009**, *31*, 300–307. [CrossRef]
8. Dabaon, M.; El-Khoriby, S.; El-Boghdadi, M.; Hassanein, M.F. Confinement effect of stiffened and unstiffened concrete-filled stainless steel tubular stub columns. *J. Constr. Steel Res.* **2009**, *65*, 1846–1854. [CrossRef]
9. Ellobody, E. Nonlinear behavior of concrete-filled stainless steel stiffened slender tube columns. *Thin-Walled Struct.* **2007**, *45*, 259–273. [CrossRef]
10. Uy, B.; Tao, Z.; Han, L.H. Behaviour of short and slender concrete-filled stainless steel tubular columns. *J. Constr. Steel Res.* **2011**, *67*, 360–378. [CrossRef]
11. Lam, D.; Gardner, L.; Burdett, M. Behaviour of axially loaded concrete filled stainless steel elliptical stub columns. *Adv. Struct. Eng.* **2010**, *13*, 493–500. [CrossRef]
12. Dai, X.; Lam, D. Axial compressive behaviour of stub concrete-filled columns with elliptical stainless steel hollow sections. *Steel Compos. Struct. Int. J.* **2010**, *10*, 517–539. [CrossRef]

13. Tao, Z.; Uy, B.; Liao, F.Y.; Han, L.H. Nonlinear analysis of concrete-filled square stainless steel stub columns under axial compression. *J. Constr. Steel Res.* **2011**, *67*, 1719–1732. [CrossRef]
14. Gunawardena, Y.; Aslani, F. Static flexural behaviour of concrete-filled spiral-welded stainless-steel tubes. *Thin-Walled Struct.* **2020**, *151*, 106731. [CrossRef]
15. He, A.; Liang, Y.; Zhao, O. Flexural buckling behaviour and resistances of circular high strength concrete-filled stainless steel tube columns. *Eng. Struct.* **2020**, *219*, 110893. [CrossRef]
16. Hassanein, M.F.; Shao, Y.B.; Elchalakani, M.; El Hadidy, A.M. Flexural buckling of circular concrete-filled stainless steel tubular columns. *Mar. Struct.* **2020**, *71*, 102722. [CrossRef]
17. Patel, V.I.; Liang, Q.Q.; Hadi, M.N.S. Nonlinear analysis of circular high strength concrete-filled stainless steel tubular slender beam-columns. *Eng. Struct.* **2017**, *130*, 1–13. [CrossRef]
18. Patel, V.I.; Liang, Q.Q.; Hadi, M.N.S. Nonlinear analysis of biaxially loaded rectangular concrete-filled stainless steel tubular slender beam-columns. *Eng. Struct.* **2017**, *140*, 120–133. [CrossRef]
19. Gunawardena, Y.; Aslani, F. Behaviour and design of concrete-filled spiral-welded stainless-steel tube short columns under concentric and eccentric axial compression loading. *J. Constr. Steel Res.* **2019**, *158*, 522–546. [CrossRef]
20. Zhong, Y.K.; Zhao, O. Behaviour of eccentrically loaded circular recycled aggregate concrete-filled stainless steel tube stub columns. *J. Constr. Steel Res.* **2022**, *198*, 107568. [CrossRef]
21. Tang, H.Y.; Hou, L.J.; Yuan, Z.Y.; Wang, Y.Z. Eccentric compressive behavior of square concrete-filled stainless steel tube (CFSST) stub columns. *Structures* **2023**, *55*, 1920–1935. [CrossRef]
22. Yousuf, M.; Uy, B.; Tao, Z.; Remennikov, A.; Liew, J.R. Transverse impact resistance of hollow and concrete filled stainless steel columns. *J. Constr. Steel Res.* **2013**, *82*, 177–189. [CrossRef]
23. Zheng, Y.; He, C.; Zheng, L. Experimental and numerical investigation of circular double-tube concrete-filled stainless steel tubular columns under cyclic loading. *Thin-Walled Struct.* **2018**, *132*, 151–166. [CrossRef]
24. Han, L.H.; He, S.H.; Liao, F.Y. Performance and calculations of concrete filled steel tubes (CFST) under axial tension. *J. Constr. Steel Res.* **2011**, *67*, 1699–1709. [CrossRef]
25. Li, W.; Han, L.H.; Chan, T.M. Performance of concrete-filled steel tubes subjected to eccentric tension. *J. Struct. Eng.* **2015**, *141*, 04015049. [CrossRef]
26. Zhou, M.; Fan, J.S.; Tao, M.X.; Nie, J.G. Experimental study on the tensile behavior of square concrete-filled steel tubes. *J. Constr. Steel Res.* **2016**, *121*, 202–215. [CrossRef]
27. Li, W.; Han, L.H.; Chan, T.M. Tensile behaviour of concrete-filled double-skin steel tubular members. *J. Constr. Steel Res.* **2014**, *99*, 35–46. [CrossRef]
28. Li, W.; Han, L.H.; Chan, T.M. Numerical investigation on the performance of concrete-filled double-skin steel tubular members under tension. *Thin-Walled Struct.* **2014**, *79*, 108–118. [CrossRef]
29. Wang, Z.B.; Yu, Q.; Tao, Z. Behaviour of CFRP externally-reinforced circular CFST members under combined tension and bending. *J. Constr. Steel Res.* **2015**, *106*, 122–137. [CrossRef]
30. Han, L.H.; Wang, Z.B.; Xu, W.; Tao, Z. Behavior of concrete-encased CFST members under axial tension. *J. Struct. Eng.* **2016**, *142*, 04015149. [CrossRef]
31. Chen, J.; Wang, J.; Jin, W. Concrete-filled steel tubes with reinforcing bars or angles under axial tension. *J. Constr. Steel Res.* **2017**, *133*, 374–382. [CrossRef]
32. Xu, L.Y.; Tao, M.X.; Zhou, M. Analytical model and design formulae of circular CFSTs under axial tension. *J. Constr. Steel Res.* **2017**, *133*, 214–230. [CrossRef]
33. Ye, Y.; Li, W.; Liu, X.J.; Guo, Z.X. Behaviour of concrete-filled steel tubes with concrete imperfection under axial tension. *Mag. Concr. Res.* **2021**, *73*, 743–756. [CrossRef]
34. Xie, W.C.; Ye, Y.; Jiang, H.; Chen, Y.W. Numerical investigation and calculation method of concrete-filled bimetallic tubes subjected to concentric tension. *Structures* **2023**, *56*, 104910. [CrossRef]
35. Ye, Y.; Li, W.; Guo, Z.X. Performance of concrete-filled stainless steel tubes subjected to tension: Experimental investigation. *Thin-Walled Struct.* **2020**, *148*, 106602. [CrossRef]
36. Ye, Y.; Yao, X.H.; Guo, Z.X. Performance of concrete-filled stainless steel tubes subjected to concentric tension: Numerical investigation and parametric study. *Structures* **2021**, *32*, 2222–2231. [CrossRef]
37. Feng, R.; Chen, Y.; He, K.; Wei, J.; Chen, B.; Zhang, X. Push-out tests of concrete-filled stainless steel SHS tubes. *J. Constr. Steel Res.* **2018**, *145*, 58–69. [CrossRef]
38. Han, L.H.; Yao, G.H.; Tao, Z. Performance of concrete-filled thin-walled steel tubes under pure torsion. *Thin-Walled Struct.* **2007**, *45*, 24–36. [CrossRef]
39. *ACI 318-11*; Building Code Requirements for Structural Concrete (ACI 318-11) and Commentary. American Concrete Institute: Indianapolis, IN, USA, 2011.
40. Hibbitt, Karlsson, & Sorensen, Inc. *ABAQUSPStandard User's Manual, version 6.5*; Hibbitt, Karlsson, & Sorensen, Inc.: Johnston, RI, USA, 2005.
41. Hillerborg, A.; Modéer, M.; Petersson, P.E. Analysis of crack formation and crack growth in concrete by means of fracture mechanics and finite elements. *Cem. Concr. Res.* **1976**, *6*, 773–781. [CrossRef]

42. Shen, J.M.; Wang, C.Z.; Jiang, J.J. *Finite Element Method of Reinforced Concrete and Limited Analysis of Plates and Shells*; Tsinghua University Press: Beijing, China, 1993. (In Chinese)
43. Rasmussen, K.J.R. Full-range stress–strain curves for stainless steel alloys. *J. Constr. Steel Res.* **2003**, *59*, 47–61. [CrossRef]
44. Ashraf, M.; Gardner, L.; David, A. Nethercot. Finite element modelling of structural stainless steel cross-sections. *Thin-Walled Struct.* **2006**, *44*, 1048–1062. [CrossRef]
45. *DBJ/T13-51-2010*; Technical Specifications for Concrete-Filled Steel Tubular Structures (Revised Version). Housing and Urban-Rural Development Department of Fujian Province: Fuzhou, China, 2010. (In Chinese)